Transition Metal-Doped C$_{20}$ Fullerene-Based Single-Atom Catalysts with High Catalytic Activity for Hydrogen Dissociation Reaction

Sehrish Sarfaraz, Muhammad Yar, Nadeem S. Sheikh,* Imene Bayach,* and Khurshid Ayub*

ACCESS | Metrics & More | Article Recommendations | SI Supporting Information

ABSTRACT: Hydrogen dissociation is a key step in almost all hydrogenation reactions; therefore, an efficient and cost-effective catalyst with a favorable band structure for this step is highly desirable. In the current work, transition metal-based C$_{20}$ (M@C$_{20}$) complexes are designed and evaluated as single-atom catalysts (SACs) for hydrogen dissociation reaction (HDR). Interaction energy (E_{int}) analysis reveals that all the M@C$_{20}$ complexes are thermodynamically stable, whereas the highest stability is observed for the Ni@C$_{20}$ complex ($E_{int} = -6.14$ eV). Moreover, the best catalytic performance for H$_2$ dissociation reaction is computed for the Zn@C$_{20}$ catalyst ($E_{ads} = 0.53$ eV) followed by Ti@C$_{20}$ ($E_{ads} = 0.65$ eV) and Sc@C$_{20}$ ($E_{ads} = 0.76$ eV) among all considered catalysts. QTAIM analyses reveal covalent or shared shell interactions in H$_2$* + M@C$_{20}$ systems, which promote the process of H$_2$ dissociation over M@C$_{20}$ complexes. NBO and EDD analyses declare that transfer of charge from the metal atom to the antibonding orbital of H$_2$ causes dissociation of the H−H bond. Overall outcomes of this study reveal that the Zn@C$_{20}$ catalyst can act as a highly efficient, low-cost, abundant, and precious metal-free SAC to effectively catalyze HDR.
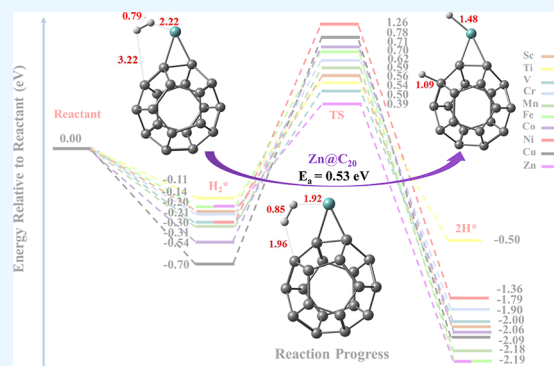
1. INTRODUCTION

Catalysts are currently viewed as the backbone of various commercial energy conversion procedures and industrial processes.[1] Nowadays, the catalyst technology is controlling the annual production of trillion dollars of goods in the food, petroleum, power, and chemical industries.[2] In this regard, noble metals are displaying exceptional catalytic activity for energy production and have outshined all traditionally used catalysts. Despite their widespread application, there are certain associated challenges with noble metal-based catalysts, i.e., their high cost and limited availability.[3−5] The scarcity and high cost of many promising noble metal catalysts such as platinum and palladium reduce their extensive utilization from the economical perspective.[6,7] To cope with this issue, various catalysts are being explored with the main motive of designing commercially viable catalysts with uncompromised catalytic activity.

The alternative approaches that are being considered have the main aim to minimize the quantity of these precious noble metals with improved or at least maintained catalytic efficiency.[8] In this regard, single-atom catalysis has emerged as a novel approach in the field of catalysis due to exceptional catalytic activity and maximal utilization efficiency. Single-atom catalysis is considered as an economically viable strategy toward performance enhancement and reduction of noble metal consumption.[9−11] Single-atom catalysis usually deals with evenly distributed metal catalysts on supports. Various synthetic procedures have been adopted with the passage of

time to design such catalysts. The techniques that are frequently used to synthesize single-atom catalysts (SACs) are wet atomic layer deposition,[12] wet chemistry,[13] and mass-selected soft landing.[14] The catalytic performance of these SACs is taking hold; however, their understanding is still limited. Hence, the study of single-metal atom-supported catalysts is highly intriguing.[15]

Hydrogen is considered as "the fuel of future" and an energy carrier due to its high potential as an ecofriendly energy source. Although the hydrogen technology has large-scale application, its practical implications have to be realized yet.[16] One of the main obstacles in the way of the hydrogen technology is cheap and effective hydrogen storage strategies.[17] In this regard, hydrogen dissociation reaction (HDR) is regarded as the key step in the H$_2$ storage process. Furthermore, HDR over metal surfaces is frequently taken as a prototype system for investigating the gas surface interactions and their catalytic understanding essence due to the simplicity of reaction.[18] Moreover, all catalytic hydrogenations involve HDR, which is considered as one of the largest classes of heterogeneous

catalysis and is very crucial for various industrial processes. Hydrogenation reactions also display a major contribution (about 6%) to chemical processes with regard to market sales in the catalytic world.[19] Metal-supported catalysts have been extensively used as catalysts for this reaction because of their suitable electronic structures, which allow H_2 molecules to get easily adsorbed and dissociated on the metallic surface.[18]

Previously, several noble metal-based SACs such as Pd,[20] Pt,[21] Rh,[22] etc., have been extensively reported in the literature to catalyze the hydrogen dissociation reaction. However, the major obstacles with these noble metal SACs include high cost, high operation temperature, and thus, lack of economic feasibility.[23] Replacing noble metals with a low-cost material is necessary for large-scale and practical application. The boron-decorated graphitic-carbon nitride B/g-C_3N_4 surface has been investigated as a cheap single-atom catalyst for the reduction of nitrogen (N_2) into NH_3.[24] Transition metals such as Mn, Fe, Ni, Co, Zn, Cu, etc., have gained much interest due to their relatively high abundance and low cost.[25,26]

On the contrary, the carbon-based materials, organic frameworks,[27] graphyne,[28] graphene,[29] graphitic carbon nitride (g-C_3N_4),[30] and porous and other nanostructured materials have received considerable attention as adsorbents (support materials for catalysts) due to their promising H_2 storage capacities, large surface areas at low temperature, and potential thermal and electronic properties.[31,32] Yan et al. investigated the Pd-doped graphene surface for hydrogen dissociation reaction during the hydrogenation of 1,3-butadiene. They observed that dissociation of H_2 occurred over the Pd atom (for subsequent hydrogenation) with a moderate energy barrier of 0.84 eV.[33] Moreover, recently, dissociation of H_2 on abundant and low-cost transition metals (Fe, Co, and Ni) supported over the C_2N surface has been investigated through the density functional theory approach.[8] However, scientists are still trying to search and design more efficient catalysts that could offer more selectivity, stability, and economical way for hydrogen dissociation reaction.

Although several experimental and DFT investigations have been previously reported for hydrogen energy applications in various carbon-based nanostructures,[34,35] very less work is considered so far for the C_{20} nanocage, "the world's smallest caged fullerene".[36] Therefore, the current study intends to choose HDR as a probe reaction to evaluate the influence of first-row transition metals supported on world's smallest cage C_{20} fullerenes as SACs and their catalytic performance. Nowadays, quantum chemical-based density functional theory (DFT) simulations are considered as the highly effective approach to evaluate the nature of a catalyst and corresponding catalytic efficiency.[37–39] Hence, the density functional theory calculation method is adopted to systematically probe the hydrogen dissociation on transition metal (M = Sc–Zn)-doped C_{20} fullerenes as SACs to elucidate the catalytic performance of designed catalysts. Furthermore, the designed catalysts are investigated for stability, improved hydrogen adsorption capacity, and their catalytic activity for hydrogen dissociation reaction. Additionally, natural bond orbital (NBO) and electron density difference (EDD) analyses are also evaluated to get further insight into the activation of the dissociation process and mode of charge transfer upon dissociation.

2. METHODOLOGY

All the simulations in the current study were performed through density functional theory implemented with the Gaussian 09 package.[40] Ground-state optimizations were performed using the B3LYP/6-31G(d,p) level of theory. B3LYP is a hybrid DFT-based functional known for quantum chemical computation of thermodynamic stabilities and electronic properties of chemical compounds.[41–43] Moreover, B3LYP is a reliable functional frequently adopted for geometry optimizations as well as mechanistic studies.[44–46] For structure visualization, GaussView 5.0, VMD, and Chemcraft were used.[47–49] Geometry optimization was confirmed via frequency analysis, i.e., the absence of imaginary or negative frequency confirms the minima nature of stationary points (reactants and products) of all studied M@C_{20} complexes. Moreover, the presence of one negative or imaginary frequency marks the confirmation of the transition state. Transition states were also evaluated via associated eigenvectors that correspond to the motion along the reaction coordinates.[50] The first-row transition metals (Sc–Zn) were doped over the C_{20} nanocage and employed to catalyze the hydrogen dissociation reaction. To get the most stable M@C_{20} configurations, transition metals were doped exohedrally at different positions over C_{20} fullerene. The first four possible spin states of considered transition metals were optimized to get the most stable spin state. The interaction energy analysis and hydrogen dissociation reactions over designed M@C_{20} complexes were carried out on the most stable spin state at the same level of theory. Interaction energies (E_{int}) of designed M@C_{20} complexes are calculated by using the following equation:

$$\Delta E_{int} = E_{M@C20} - (E_{C20} + E_M) \tag{1}$$

Here, $E_{M@C20}$ refers to the energy of the complex, whereas E_{C20} and E_M are the energies of the isolated C_{20} nanocage and transition metal atom with the most stable spin state, respectively.

The adsorption energy ΔE_{ads} of hydrogen is also calculated by using eq 2 to further estimate the adsorption capacity of designed complexes. In eq 2, $E_{H2M@C20}$ refers to the total energy of the H_2-adsorbed M@C_{20} complex, E_{H2} refers to the energy of individual H_2 molecule, and $E_{M@C20}$ corresponds to the energy of designed M@C_{20} complexes.

$$\Delta E_{ads} = E_{H2M@C20} - (E_{M@C20} + E_{H2}) \tag{2}$$

The reaction energy (ΔE) and activation energy barrier (E_a) are computed according to eqs 3 and 4, respectively, where E_R, E_{TS}, and E_P represent the energies of the reactants (R), transition state (TS), and the product or final state (P), respectively. The reaction pathways and mechanism of the hydrogen dissociation reaction were determined by comparing the activation energy barriers (E_a).[51]

$$\Delta E = E_P - E_R \tag{3}$$

$$E_a = E_{TS} - E_R \tag{4}$$

To explore the knowledge of the donor–acceptor interactions, the mechanism of dissociation of the H_2 molecule over designed complexes was further evaluated via EDD and NBO analyses. NBO analysis was carried out at the B3LYP/6-31G(d,p) level of theory, which elaborates the nature of bonding in terms of charge transfer and orbital interactions. Moreover, to get a clearer idea of the nature of interatomic

interactions, quantum theory of atoms in molecules (QTAIM) or topological analyses were performed via the Multiwfn 3.8 program.

3. RESULTS AND DISCUSSION

3.1. Geometry Optimization and Adsorption Energy.
The designed M@C$_{20}$ complexes are optimized to their most stable geometry prior to the hydrogen adsorption and evaluated using the B3LYP/6-31G(d,p) level of theory. The titled nanocage of interest, C$_{20}$ fullerene, consists of 12 five-membered fused rings with an average C—C bond length of 1.44 Å (b5,5 bond), consistent with the reported one.[52] The computed geometry of C$_{20}$ fullerene at both top and side views is presented in Figure 1. Moreover, the first-row transition
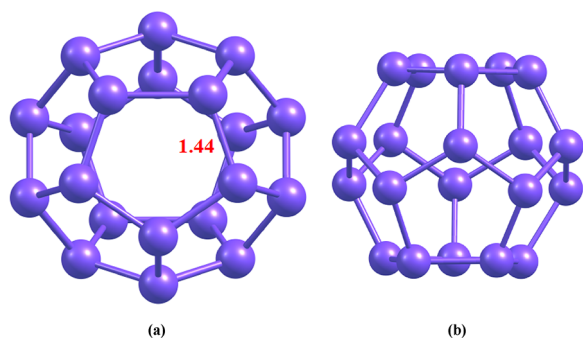

Figure 1. Top view (a) and side view (b) of the optimized structure of the C$_{20}$ nanocage with the average C—C bond length mentioned at the B3LYP/6-31G(d,p) level of theory.

metal atoms are exohedrally doped over the C$_{20}$ nanocage at various doping sites, i.e., on the top of pentagons and at the b5,5 interface. In all the considered M@C$_{20}$ complexes, the most stable complex is observed on the b5,5 interface. The first four possible spin states of the designed M@C$_{20}$ complexes are optimized using DFT spin-polarized quantum chemical simulations to get the lowest and most stable possible geometry. The relative energies of the first four possible spin states of M@C$_{20}$ complexes in eV are listed in Table S1 (Supporting Information). Among studied complexes, doublet is the most stable spin state for Sc@C$_{20}$ and Cu@C$_{20}$, quartet for V@C$_{20}$ and Co@C$_{20}$, and sextet for the Mn@C$_{20}$ complex, whereas the most stable spin state for Ti@C$_{20}$ is triplet, that for Cr@C$_{20}$ and Fe@C$_{20}$ is quintet, and that for Ni@C$_{20}$ and Zn@C$_{20}$ is singlet. All the designed M@C$_{20}$ complexes are optimized at zero charge. The lowest energy spin states are considered as the most stable one and are used in this study for discussion hereafter.

The ground-state optimized geometries along with C—M bond lengths of designed complexes are given in Figure 2, and their corresponding interaction energies are given in Table 1. From Figure 2, it is obvious that the interaction bond distances between the carbon atom of C$_{20}$ fullerene and the transition metal are observed in the range of 1.82 to 2.10 Å, which principally reveal chemisorption. The lowest interaction distance is calculated for the Ni@C$_{20}$ complex (1.82 Å) for each Ni—C bond, followed by the Zn@C$_{20}$ complex (1.85 Å). In the case of the Ni@C$_{20}$ complex, the lowest bond value is also justified from the highest interaction energy (ΔE_{int}) value of −6.14 eV, whereas the highest value of interaction distance of 2.10 Å is calculated for the Sc@C$_{20}$ complex for each Sc—C bond among all designed complexes. It is further observed that

interaction bond distance values are gradually decreased with the increase in atomic number from Sc to Zn. The calculated interaction distance values between C$_{20}$ fullerene and the transition metal atom are almost similar when compared with the previously reported M—C bond lengths.[53]

Besides interaction distance, another important parameter to evaluate the stability is interaction energy. The interaction energy of M@C$_{20}$ complexes is calculated using eq 1, and the interaction energy values in different spin states are related to their unpaired electrons present (see Table 1). The negative sign of interaction energy values reveals that transition metal atom doping over the C$_{20}$ nanocage is a facile process for all metal atoms (Sc—Zn). Among all studied M@C$_{20}$ complexes, the highest value of interaction energy is computed for the Ni@C$_{20}$ complex, revealing the corresponding thermodynamic stability of this complex. The highest E_{int} value of the Ni@C$_{20}$ complex is very nicely correlated with the shortest bond length of the M—C bond (see Figure 2). The E_{int} values in the range of −1.53 to −6.14 eV are calculated for all considered complexes, which further confirm the stability of designed complexes. Overall, no post-optimization structural deformation is observed in any complex (see Figure 2). The results of interaction energy analysis are also validated through interaction distances of the M—C bond of M@C$_{20}$ complexes.

3.2. H$_2$ Adsorption over M@C$_{20}$ Catalysts.
The adsorption energy (E_{ads}) of an adsorbed atom or molecule is defined as the amount of energy required for an adsorbed atom to get desorbed from the surface. Thus, adsorption is an exothermic surface-based reaction that liberates energy when a gas atom or molecule is adsorbed on a surface.[54] Initially, the hydrogen molecule is adsorbed over the top of the transition metal as well as from the side edge of the complex, and the side edge position is energetically more favorable for hydrogen adsorption in all catalysts. Hence, adsorption energy on average has been computed for the adsorption of the hydrogen molecule on the side edge position in all designed surfaces (see Figure 3). Adsorption energy (E_{ads}) for the H$_2$ adsorption over M@C$_{20}$ complexes is also computed and listed in Table 1. The more negative the E_{ads} is, the more strongly and rigidly bound the adhered hydrogen atom is to the catalyst surface, which corresponds to a favorable adsorption and exothermic process, whereas the positive E_{ads} value corresponds to an unfavorable adsorption and endothermic process. Therefore, the higher the E_{ads} value is, the H$_2$-adsorbed M@C$_{20}$ system has higher stability. In all 10 designed complexes, the hydrogen adsorption process is energetically favorable without any distortion in the structure and computed adsorption energy values are seen in the range of −0.01 to −0.71 eV. Furthermore, the Cu@C$_{20}$ (−0.71 eV) and Co@C$_{20}$ (−0.54 eV) catalysts relatively show strong H$_2$ adsorption (for details, check Table 1). The negative adsorption energy values show that H$_2$ adsorption over M@C$_{20}$ catalysts is a facile process. It is further observed that the H$_2$ molecule approaches the designed catalysts from the side view location in all studied systems. Similarly, the H—H bond distance upon adsorption of the hydrogen molecule over designed M@C$_{20}$ catalysts is observed in the range of 0.77 to 0.84 Å as mentioned in Figure 3. In the case of some complexes, a slightly larger H—H bond distance is observed as compared to the isolated H$_2$ molecule, i.e., 0.74 Å, which is mainly attributed to strong C—H and M—H bond interactions, and hence ultimately results in weakening of the H—H bond. Moreover, the M—H interaction distances vary from 2.22 to 3.34 Å, whereas C—H interaction distances
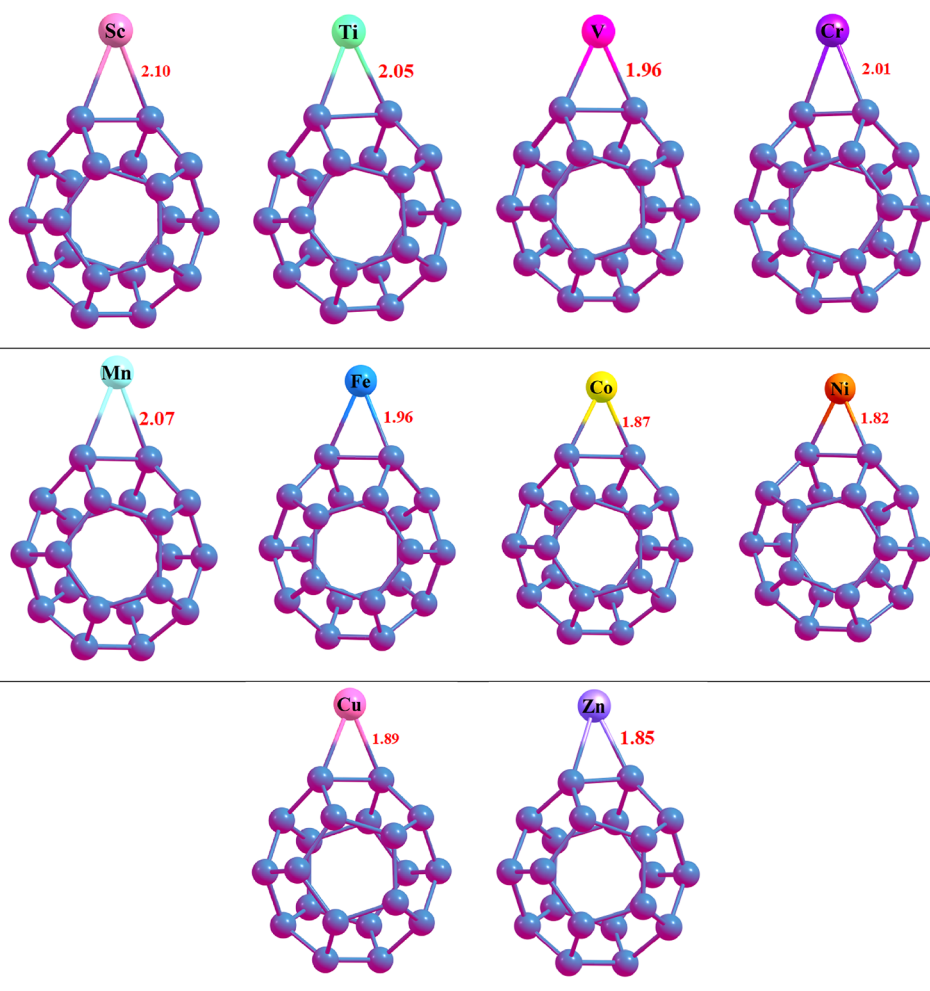
Figure 2. Optimized structures of stable M@C$_{20}$ complexes (M = Sc−Zn) with M−C bond distances mentioned at the B3LYP/6-31G(d,p) level of theory.

Table 1. Summary of Energies for the Interaction of the Transition Metal (M) Atom over the C$_{20}$ Nanocage (ΔE_{int}), H$_2$ Adsorption Energies of H$_2$M@C$_{20}$ (ΔE_{ads}), and Activation Barriers (ΔE_a) for Hydrogen Dissociation Reaction

complex	ΔE_{int} (eV)	complex	ΔE_{ads} (eV)	ΔE_a (eV)
Sc@C$_{20}$	−2.98	H$_2$Sc@C$_{20}$	−0.20	0.76
Ti@C$_{20}$	−3.09	H$_2$Ti@C$_{20}$	−0.11	0.65
V@C$_{20}$	−2.82	H$_2$V@C$_{20}$	−0.30	0.80
Cr@C$_{20}$	−3.24	H$_2$Cr@C$_{20}$	−0.21	0.83
Mn@C$_{20}$	−1.53	H$_2$Mn@C$_{20}$	−0.31	0.90
Fe@C$_{20}$	−2.08	H$_2$Fe@C$_{20}$	−0.14	0.84
Co@C$_{20}$	−2.64	H$_2$Co@C$_{20}$	−0.54	1.25
Ni@C$_{20}$	−6.14	H$_2$Ni@C$_{20}$	−0.30	1.56
Cu@C$_{20}$	−3.46	H$_2$Cu@C$_{20}$	−0.71	1.49
Zn@C$_{20}$	−2.93	H$_2$Zn@C$_{20}$	−0.14	0.53

are calculated in the range of 1.72 to 3.53 Å in all studied complexes (see Figure 3).

Overall, the lowest value of adsorption energy among all studied M@C$_{20}$ catalysts is seen in the Ti@C$_{20}$ catalyst (−0.11 eV), whereas the highest adsorption energy value is observed for Cu@C$_{20}$ catalysts (−0.71 eV). Overall, the adsorption of the hydrogen molecule over M@C$_{20}$ nanocages slightly

increases the H−H bond length and hence reveals the activation of the hydrogen molecule over designed catalysts.

3.3. Hydrogen Dissociation Reaction over M@C$_{20}$ Complexes. Dissociative adsorption of the hydrogen molecule is one of the prominent reactions on catalytic surfaces, since this reaction requires the cleavage of a covalent molecular bond and simultaneously involves the creation of new chemical bonds (atomic nature). Therefore, the hydrogen-adsorbed M@C$_{20}$ complexes are analyzed. To evaluate the best performance of the considered M@C$_{20}$ catalysts for the catalytic dissociation of the H$_2$ molecule, the heterolytic dissociation pathway of the hydrogen-adsorbed complexes is studied. An activation energy or energy barrier (E_a) is considered as a potential field that can act as an important criterion to either regulate or localize the transference of charged particles (electrons).[55] Therefore, an energy barrier (E_a) should be overcome to start the transport of charges from the electron donor site (oxidation) to the electron acceptor site (reduction).

The energetics of the hydrogen dissociation reaction (HDR) pathway over various designed M@C$_{20}$ catalysts are pictorially demonstrated in Figure 4. The free energy diagram declares that both H$_2$* and 2H* states are energetically favorable in the case of all the designed M@C$_{20}$ catalysts, which is confirmed from the associated negative energy (see Figure 4), unveiling the thermodynamic stability of these states. The catalytic
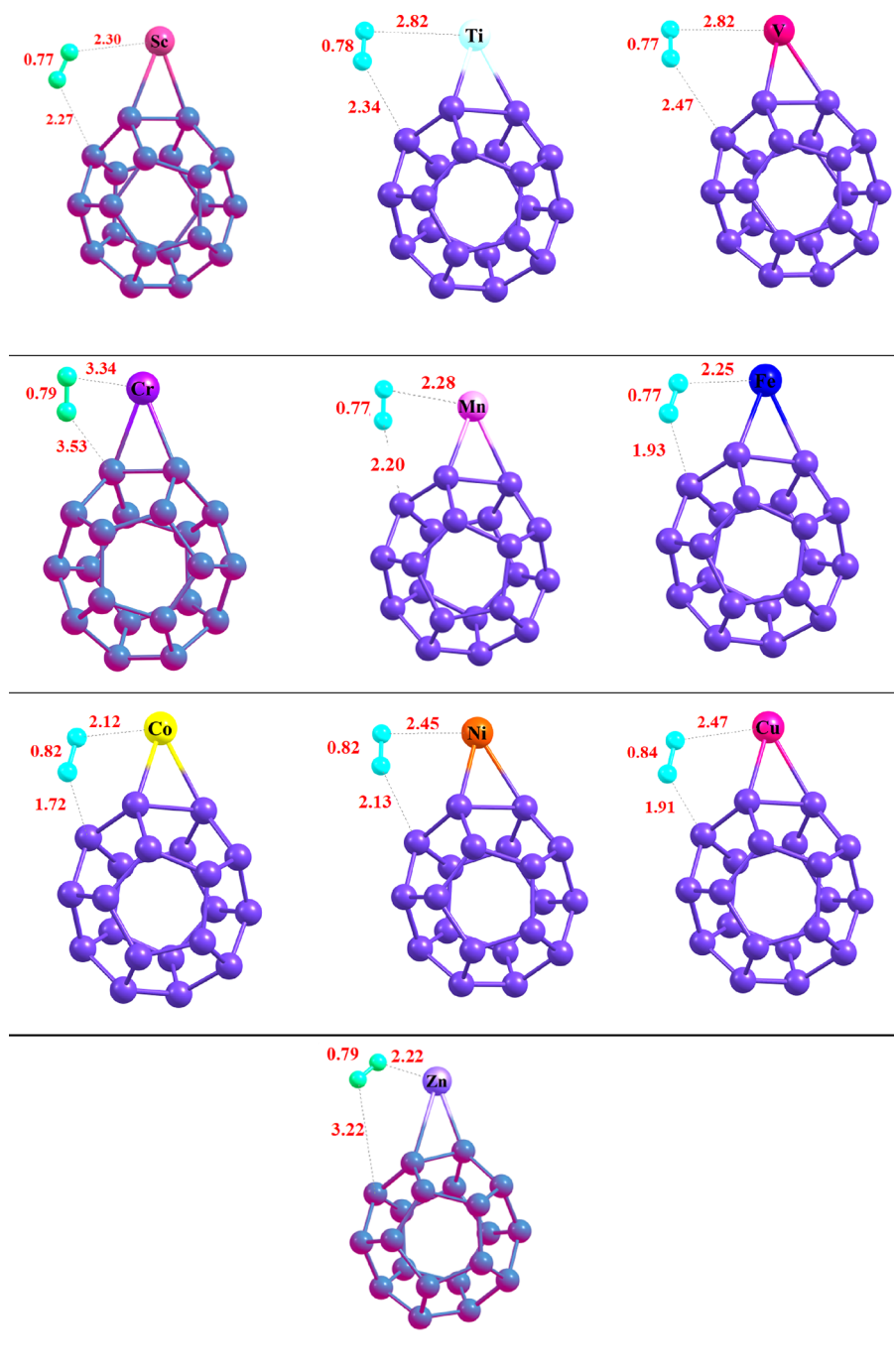
Figure 3. Optimized structures of hydrogen-adsorbed M@C_{20} complexes (M = Sc−Zn) with important interaction distances mentioned at the B3LYP/6-31G(d,p) level of theory.

dissociation process of the H_2 molecule has three steps: the first step involves the adsorption of the H_2 molecule, giving an intermediate, followed by the second step, which involves the cleavage H−H bond of the hydrogen molecule and, finally, binding of atomic hydrogen on the corresponding binding sites.

Among considered hydrogen-adsorbed M@C_{20} complexes, the lowest dissociation barrier is calculated for the Zn@C_{20} catalyst (0.53 eV), whereas in the case of the Ni@C_{20} catalyst, the highest energy barrier of 1.56 eV is observed. Furthermore, the lowest energy barrier of the Zn@C_{20} catalyst is followed by Ti@C_{20} and Sc@C_{20} catalysts with activation barriers of 0.65

and 0.76 eV, respectively. The energy barriers for the dissociation of the H_2 molecule over V@C_{20} and Cr@C_{20} are also comparably smaller with values of 0.80 and 0.83 eV, respectively. For the rest of the considered catalysts, the energy barriers are 0.84, 0.90, 1.25, 1.48, and 1.56 eV for Fe@C_{20}, Mn@C_{20}, Co@C_{20}, Cu@C_{20}, and Ni@C_{20}, respectively. The H−H bond distances at the transition state vary between 0.77 and 0.84 Å, which reveals that the H−H bond distances increase upon activation and facile splitting of the H_2 molecule. Similarly, the C−H and M−H interaction bond distances are reduced at the transition state as compared to the intermediate state (see Figure 5).
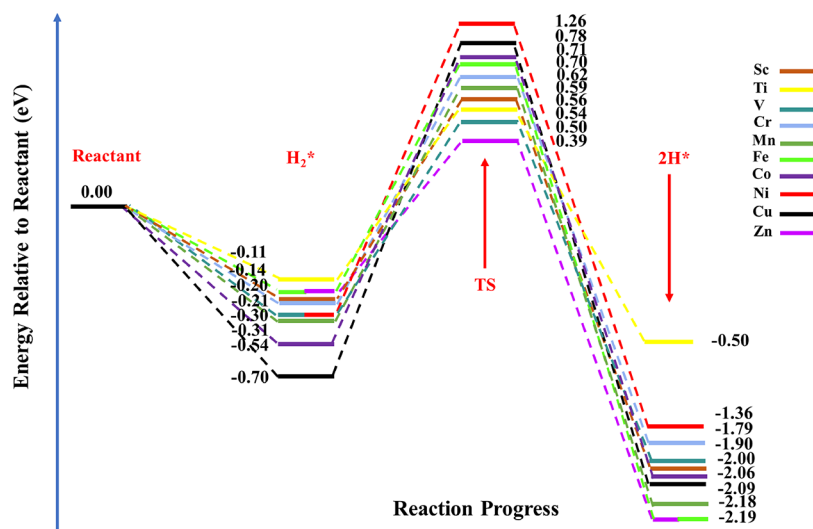
Figure 4. Hydrogen dissociation reaction (HDR) pathway on M@C$_{20}$ (M = Sc−Zn) complexes. The energies of intermediate (H$_2$*), transition state (TS), and products (2H*) are relative to reactants and are expressed in units of eV.

Herein, the catalysts with better efficiency, i.e., Zn@C$_{20}$, Ti@C$_{20}$, and Sc@C$_{20}$ catalysts, are considered as representative models for the detailed investigation of hydrogen dissociation reaction. Additionally, all these M@C$_{20}$ complexes with better catalytic efficiency (Zn@C$_{20}$, Ti@C$_{20}$, and Sc@C$_{20}$) are given in Figure 5, whereas energy diagrams of the rest of studied M@C20 complexes are given in the Supporting Information (Figure S1a−g). As shown in Figure 5a, on the Zn@C$_{20}$ surface, for hydrogen dissociation reaction (H$_2$* → 2H*), initially, the reactant H$_2$ is adsorbed at the side edge position where one hydrogen atom is approaching toward Zn and the other toward the carbon atom. Then, the dissociation of the hydrogen molecule resulted in the formation of two H atoms, which adsorbed at C site and M site positions. This hydrogen dissociation step needs to overcome the activation energy barrier of 0.53 eV (12.22 kcal/mol). The H−H bond distance is a critical structural parameter in dissociation reaction, which demonstrates the stability of the transition state. In the case of the Zn@C$_{20}$ complex, the H−H bond distance at the transition state extends to 0.85 Å, which is initially at about 0.79 Å. This elongation in H−H bond length upon adsorption declares the activation of the hydrogen molecule over the Zn@C$_{20}$ complex. The transition state shows that the H$_2$ splitting process proceeds via heterolytic cleavage of the hydrogen molecule. The C−H and Zn−H interaction distances are reduced to 1.96 and 1.92 Å (transition state) from 3.22 and 2.22 Å (intermediate), respectively. The H$_2$ molecule is dissociated to give two hydrogen atoms, which on the product side migrated toward the Zn atom and C atom (see Figure 5), accompanied by the release of −2.58 eV energy. The Zn−H and C−H bond lengths upon binding are calculated as 1.48 and 1.09 Å, respectively. Moreover, the enthalpy of the product side (H$_2$Zn@C$_{20}$ complex) is −2.19 eV, hence revealing that the product is more stabilized as compared to reactants.

Similarly, the second lowest barrier is calculated for the Ti@C$_{20}$ catalyst, and the detailed free energy diagram along with pictorial representation can be seen in Figure 5b. In the case of the Ti@C$_{20}$ catalyst, the calculated C−Ti bond length is 2.05 Å between C atoms of C$_{20}$ fullerene (directly attached to Ti) and the Ti atom, which nicely correlates with the already

reported literature.[56] The H−H bond distance elongates from 0.78 (intermediate) to 0.91 Å (transition state) as presented in Figure 5b. The energy barrier calculated for hydrogen dissociation over the Ti@C$_{20}$ catalyst is 0.65 eV (14.98 kcal/mol). The C−H and Ti−H interaction distances are reduced from 2.34 and 2.82 Å to 1.57 and 2.07 Å, respectively, while moving from the intermediate state to the transition state. Upon dissociation, the hydrogen atoms bind with the metal center (Ti−H) and carbon center (C−H) with bond lengths of 1.75 and 1.09 Å, respectively.

In the case of the Sc@C$_{20}$ catalyst, the initial H−H bond length of the adsorbed hydrogen molecule is 0.77 Å, which elongates to 0.86 Å in the transition state. Just like dissociation over the Zn@C$_{20}$ surface, hydrogen dissociation also occurs on the side edge position over the Sc@C$_{20}$ catalyst. Again, the dissociated hydrogen atoms get adsorbed at C site and M site positions. The hydrogen dissociation step in this case needs to overcome the barrier of 0.76 eV (17.53 kcal/mol). The C−H and Sc−H interaction bond distances at the intermediate are 2.27 and 2.30 Å, which reduce to 1.72 and 2.12 Å at the transition state, respectively. The dissociated hydrogen atoms then bind with the metal adsorption site and carbon site independently with bond lengths of 1.83 (Sc−H) and 1.09 Å (C−H), respectively. Moreover, the enthalpy of the product side (H$_2$Sc@C$_{20}$ complex) is −2.00 eV, which reveals that overall, the product is more stabilized as compared to reactants. In above discussed complexes, the C−H bond length is consistent in all cases. The obtained results agree well with the previously reported literature for H−H bond distances over various transition metal catalysts.[57−60]

Table 1 depicts that the energy barriers for the dissociation of H$_2$ molecules over the designed M@C$_{20}$ catalysts lie in the wider range of 0.53 to 1.56 eV. Overall, the lowest energy barrier among all designed transition metal-doped C$_{20}$ complexes is calculated for the Zn@C$_{20}$ complex (0.53 eV), which can be easily attainable under mild conditions (basic requirement for the hydrogenation process). This means that the Zn@C$_{20}$ complex has the best catalytic activity for hydrogen dissociation reaction as compared to the other studied complexes. The higher catalytic activity of the Zn@C$_{20}$ complex is attributed to the higher charge density of the zinc
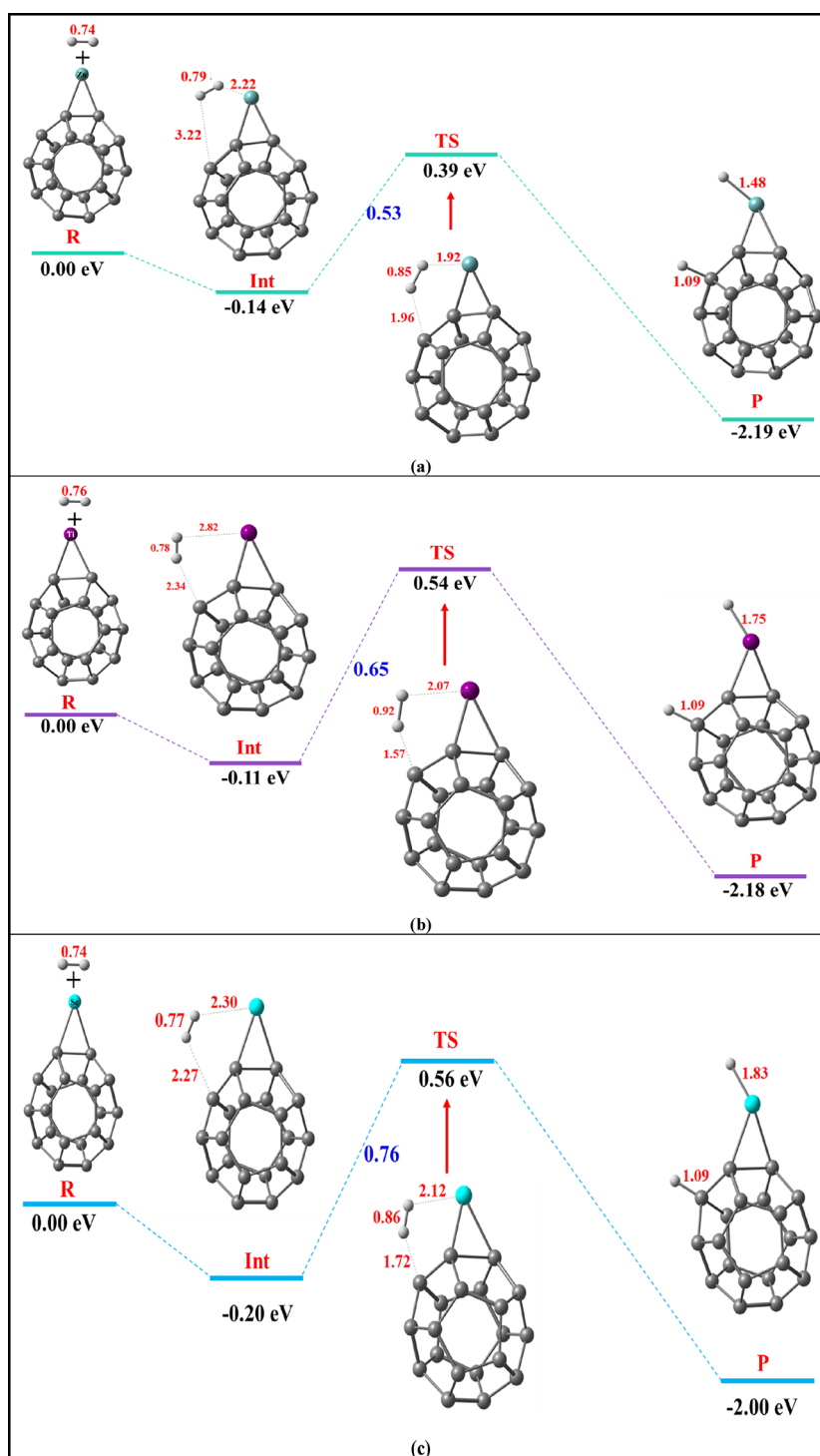
Figure 5. The schematic energy diagrams of reactant (R), intermediate (Int), transition state (TS), and product (P) are demonstrated for (a) Zn@C_{20}, (b) Ti@C_{20}, and (c) Sc@C_{20} at the B3LYP/6-31G(d,p) level of theory (H, light gray; C, gray; Zn, green; Sc, cyan blue; Ti, purple).

metal atom as compared to other studied first-row transition metals. The calculated hydrogen dissociation barrier over the Zn@C_{20} complex is much smaller than that reported for $Mg_{15}Ni_2Al_{12}$ surfaces (0.82 eV) for hydrogen dissociation.[61] Similarly, the dissociation barrier over the Zn@C_{20} complex is almost comparable with that of the noble metal-doped Au/TiO_2 system, where the energy barrier of 0.54 eV was reported in the literature.[62] Zn@C_{20} acting as a SAC delivers the best activity for hydrogen dissociation reaction; therefore, the Zn@

C_{20} catalyst can be a promising single-atom catalyst (SAC) to efficiently catalyze HDR.

3.4. QTAIM Analyses. QTAIM analyses (Bader's quantum theory of atoms in molecules) are employed to evaluate the interactions that exist between adsorbed hydrogen and the designed systems. In QTAIM analyses, the topological parameters that are helpful for explaining the nature of interactions along bond critical points are the density of electron (ρ), Laplacian of electron density ($\nabla^2\rho$), Lagrangian kinetic density ($G_{(r)}$), potential energy density ($V_{(r)}$), and total

Table 2. Obtained Results of the Topological Parameters of the Studied Hydrogen-Adsorbed M@C$_{20}$ Complexes through QTAIM Analyses at the B3LYP/6-31G(d,p) Level of Theory

| complex	analyte−C$_2$N	ρ (a.u.)	$\nabla^2\rho$ (a.u.)	$G_{(r)}$ (a.u.)	$V_{(r)}$ (a.u.)	$H_{(r)}$ (a.u.)	$-V/G$
H$_2$Sc@C$_{20}$	Sc−H1	0.032	0.102	0.024	−0.023	−0.004	−5.75
	C−H2	0.063	0.030	0.024	−0.017	−0.017	−1.00
H$_2$Ti@C$_{20}$	Ti−H1	0.034	0.105	0.027	−0.028	−0.009	−3.11
	C−H2	0.088	−0.028	0.030	−0.064	−0.033	−1.94
H$_2$V@C$_{20}$	V−H1	0.038	0.140	0.037	−0.039	−0.008	−4.88
	C−H2	0.077	−0.093	0.028	−0.053	−0.026	−2.04
H$_2$Cr@C$_{20}$	Cr−H1	0.041	−0.095	0.032	−0.040	−0.008	−5.00
	C−H2	0.089	−0.015	0.029	−0.064	−0.034	−1.88
H$_2$Mn@C$_{20}$	Mn−H1	0.039	0.059	0.025	−0.036	−0.010	−3.60
	C−H2	0.083	−0.026	0.029	−0.058	−0.029	−2.00
H$_2$Fe@C$_{20}$	Fe−H1	0.045	−0.069	0.031	−0.045	−0.014	−3.21
	C−H2	0.079	−0.041	0.028	−0.055	−0.027	−2.04
H$_2$Co@C$_{20}$	Co−H1	0.051	−0.066	0.035	−0.055	−0.019	−2.89
	C−H2	0.081	−0.013	0.029	−0.057	−0.028	−2.04
H$_2$Ni@C$_{20}$	Ni−H1	0.076	−0.145	0.073	−0.111	−0.037	−3.00
	C−H2	0.088	0.016	0.003	−0.029	−0.034	−0.85
H$_2$Cu@C$_{20}$	Cu−H1	0.067	0.114	0.059	−0.089	−0.030	−2.97
	C−H2	0.072	−0.015	0.026	−0.048	−0.022	−2.18
H$_2$Zn@C$_{20}$	Zn−H1	0.047	0.110	0.037	−0.046	−0.010	−4.60
	C−H2	0.071	−0.016	0.026	−0.048	−0.022	−2.18
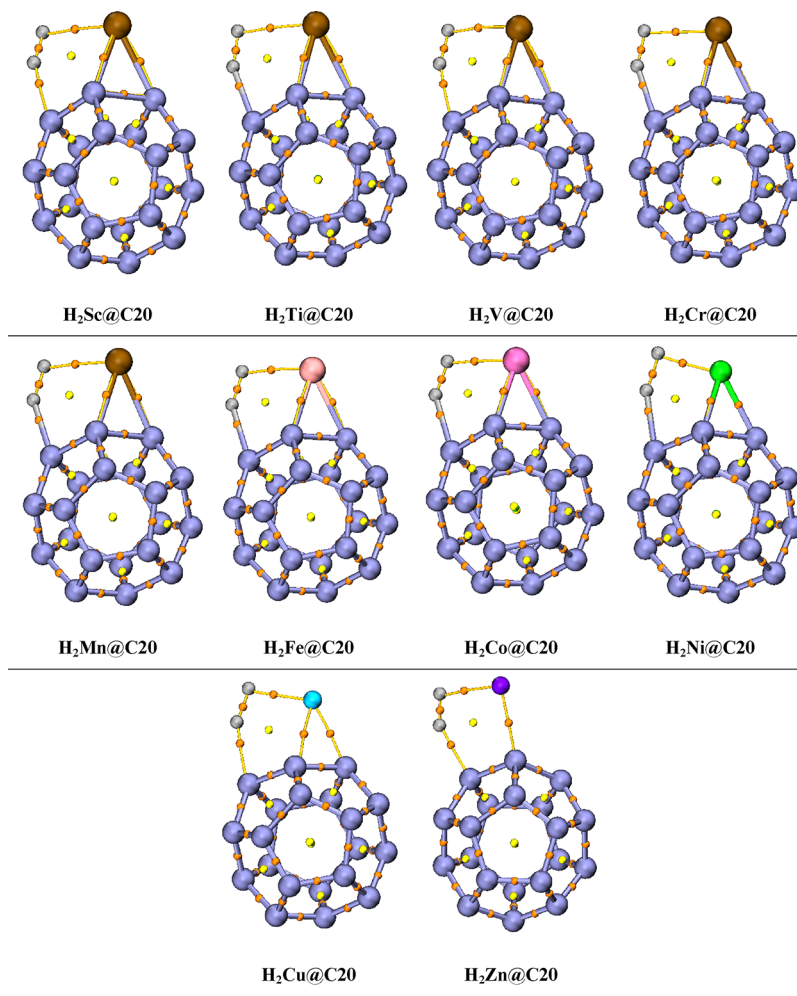
Figure 6. QTAIM molecular plots of the considered hydrogen-adsorbed M@C$_{20}$ complexes at the B3LYP/6-31G(d,p) level of theory.

electronic energy density ($H_{(r)}$). The strength of the bond can be evaluated with the help of electron density (ρ) at the bond critical point (BCP), while the nature of interaction can be characterized via Laplacian of electron density ($\nabla^2\rho$). More-

over, interatomic interactions can also be evaluated through the $-V/G$ ratio, i.e., $-V_{(r)}/G_{(r)} < 1$ corresponds to weak interactions, and $-V_{(r)}/G_{(r)} > 2$ shows covalent bonding. Therefore, the extracted values of bond critical point (BCP) parameters through QTAIM analysis are listed in Table 2, whereas the isosurfaces obtained via QTAIM analyses of the designed hydrogen-adsorbed systems are given in Figure 6.

With respect to the designed catalyst interaction with adsorbed hydrogen, two (2) BCPs are observed for each complex, as given in Table 2 and Figure 6. The value of Laplacian $(\nabla^2 \rho)$ for considered BCPs falls within the range of -0.145 to 0.140 for the hydrogen molecule-adsorbed systems $(H_2^* + M@C_{20})$. However, the value of Laplacian greater than zero $(\nabla^2 \rho > 0)$ indicates the closed shell interactions, i.e., weak interactions. Interestingly, Lagrangian kinetic energy and potential energy density values are obtained as positive and negative, respectively, which are in accordance with our designed systems in this study at all the considered BCPs. It is further observed that the total electronic energy density $(H_{(r)})$, which is equal to the sum of $G_{(r)}$ and $V_{(r)}$, has a value of $H < 0$, revealing the presence of covalency. For all the studied complexes, i.e., hydrogen molecule-adsorbed systems have a negative $H_{(r)}$ value, hence gratifying the covalent nature of interactions in the studied systems. The $-V/G$ ratio falls within the range of 0.85 to 5.75, which further confirms the finding that except few cases, all the calculated BCPs show shared shell interactions. These explicit QTAIM analysis results are superior because they confirm some bond interactions that are not possible through structural analysis. Thus, these obtained results are consistent with the calculated adsorption energies and reactivity of the studied complexes.

3.5. Electron Density Differences and Natural Bond Orbital Analyses.
The activation and dissociation of the hydrogen molecule over designed catalysts are further evaluated through electron density difference (EDD) and natural bond orbital (NBO) analyses. NBO analysis is carried out to estimate the exact amount of charge that is being transferred from the d-orbitals of first-row transition metals upon H_2 molecule adsorption. The calculated values of NBO charges on the transition metal, hydrogen atoms, and corresponding carbon atom of hydrogen-adsorbed $M@C_{20}$ complexes are listed in Table 3. In all hydrogen-adsorbed $M@C_{20}$ complexes, the transition metal atom possesses a positive value of NBO charge, whereas the corresponding hydrogen atom (H1) interacting with the transition metal bears a negative value of NBO charge. Similarly, the positive

Table 3. NBO Analysis of Considered Stable Hydrogen-Adsorbed $M@C_{20}$ Complexes at the B3LYP/6-31G(d,p) Level of Theory

complex	H1 (e)	M (e)	H2 (e)	C (e)
$H_2Sc@C_{20}$	−0.167	1.275	0.117	−0.418
$H_2Ti@C_{20}$	−0.221	1.025	0.159	−0.438
$H_2V@C_{20}$	−0.209	0.995	0.150	−0.417
$H_2Cr@C_{20}$	−0.225	0.921	0.159	−0.395
$H_2Mn@C_{20}$	−0.201	0.980	0.141	−0.434
$H_2Fe@C_{20}$	−0.206	0.929	0.149	−0.419
$H_2Co@C_{20}$	−0.208	0.859	0.153	−0.404
$H_2Ni@C_{20}$	−0.223	0.631	0.192	−0.313
$H_2Cu@C_{20}$	−0.202	0.731	0.155	−0.342
$H_2Zn@C_{20}$	−0.111	0.653	0.089	−0.458

NBO charge is seen on the hydrogen atom (H2) with the negative charge on the C atom interacting with H2. NBO analysis shows that the transition metals owing to their electropositive nature transferred the charges from the metal atom to the C_{20} nanocage and H_2 atoms. The positive NBO charge on transition metals reveals the transfer of charge from metal atoms to the C_{20} support in all designed complexes. However, on the H2 atom-interacting site, the carbon atom of the C_{20} nanocage is extracting charge from the hydrogen atom (H2). The highest NBO charge is calculated for the Sc metal (+1.275e), whereas the lowest amount of NBO charge transfer is calculated for the Ni metal (+0.631e).

Herein, we consider the detailed discussion of charge transfer of the only representative model, i.e., $H_2Zn@C_{20}$ complex. In this case, a charge of about +0.653e is examined on the Zn metal atom, whereas a charge of −0.111e is noticed over the hydrogen atom interacting toward the metal atom (H1). At the transition state, a charge of −0.458e is calculated for the representative carbon atom interacting with the adsorbed hydrogen molecule, whereas hydrogen (H2) bears a charge of +0.089e. The positive charge appears on the metal center, which indicates the electropositive character of the metal atom and the charge transfer from the Zn atom to the H atom. Similarly, the positive charge on the hydrogen (H2) atom reveals the transfer of NBO charge from the hydrogen atom to the carbon atom participating in the transition state. Overall, the charge transfer analysis unveils the strong binding interactions of the metal atom with the adsorbed H_2 molecule, thus causing the dissociation of the H_2 molecule. The transfer of charges along both interacting sites is greatly responsible for the H−H bond elongation, hence facilitating the hydrogen splitting process over $M@C_{20}$ complexes. Furthermore, NBO analysis indicates the transfer of charge from the metal atom to the H_2 molecule, resulting in filling up σ^* (antibonding orbital) of hydrogen and thus marking the dissociation of the H−H bond.

Electron density difference (EDD) is carried out to further validate the results of amount of charge transfer upon hydrogen adsorption obtained via NBO analysis. The EDD isosurfaces plotted for all studied hydrogen-adsorbed $M@C_{20}$ complexes are presented in Figure 7. The electron density difference plots exhibit violet and cyan blue patches, which therefore confirm the transfer of charges upon hydrogen adsorption. In the color scheme, violet-colored isosurfaces depict the electronic density depletion, whereas cyan blue isosurfaces show the accumulation of electron density. It is obvious from EDD that charge is transferred from the transition metal to the hydrogen atom (H1) and from H2 to the carbon atom upon hydrogen molecule adsorption in all studied $M@C_{20}$ complexes (for details, see Figure 7). In all considered complexes, the violet patches mainly appear over the transition metal atom and hydrogen atom (H2), presenting the electronic density depletion, whereas cyan blue-colored isosurfaces appear over the hydrogen atom (H1) and carbon atoms of the C_{20} nanocage. The results of EDD analysis are strongly consistent with the outcomes of charge transfer (NBO) analysis. Furthermore, this charge transfer process facilitates the process of filling up σ^* (antibonding orbital) of hydrogen and thus makes the hydrogen dissociation process more facile over $M@C_{20}$ catalysts.

Overall, transition metal-doped C_{20} complexes can act as promising single-atom catalysts (SACs) to efficiently catalyze HDR. The current study declares the $Zn@C_{20}$ complex as an
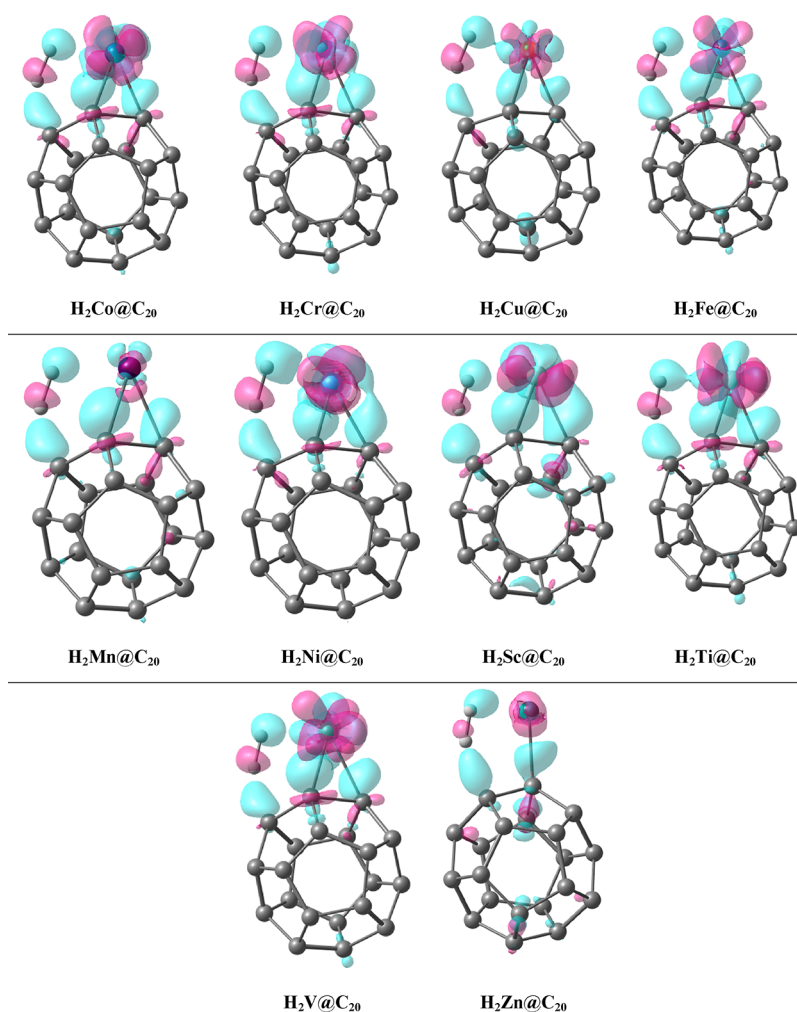
Figure 7. EDD analysis of studied $M@C_{20}$ complexes at the B3LYP/6-31G(d,p) level of theory. The cyan blue color presents electron density accumulation, whereas the violet color shows the depletion of electron density.

efficient electrocatalyst for the hydrogen splitting process with the lower energy barrier of 0.53 eV. Therefore, it provides a new avenue for scientists to design high-performance SACs based on heteroatom nanocages for the facile hydrogen dissociation process.

4. CONCLUSIONS

Herein, quantum chemical DFT investigations are carried out to systematically probe the adsorption and catalytic dissociation of the H_2 molecule over transition metal-doped C_{20} fullerene-based SACs. Transition metal adsorption over C_{20} fullerene is exothermic for all considered metals, and the highest interaction energy is computed for the $Ni@C_{20}$ complex. Moreover, the adsorption of the H_2 molecule over $M@C_{20}$ complexes and the hydrogen dissociation barriers are also systematically compared for all studied complexes. Hydrogen dissociation reaction (HDR) pathway values (Figure 5) declare that the atomic hydrogen ($2H^*$ state) for studied $M@C_{20}$ catalysts is energetically more favorable due to the exothermic process (negative energy). The lowest value of hydrogen dissociation barrier among all considered $M@C_{20}$ complexes is observed for the $Zn@C_{20}$ complex (0.53 eV). The better catalytic activity of the $Zn@C_{20}$ catalyst is attributed to the higher charge or electronic density of the Zn metal atom. Charge transfer analyses indicate the transfer of

charge from the metal atom to the H_2 molecule, resulting in filling up σ^* (antibonding orbital) of H_2 and thus making the dissociation of the H—H bond feasible. Moreover, QTAIM analyses are performed to evaluate the nature of interaction and results show that covalent or shared shell interactions exist in $H_2^* + M@C_{20}$ systems, which promote the process of H_2 dissociation over $M@C_{20}$ complexes. Overall, the current study declares the $Zn@C_{20}$ complex as an efficient electrocatalyst for HDR and thus opens a new avenue for researchers to design high-performance SACs for facile hydrogen dissociation.

■ ASSOCIATED CONTENT

ⓢ Supporting Information

The Supporting Information is available free of charge at https://pubs.acs.org/doi/10.1021/acsomega.3c00721.

> Relative stabilities of $M@C_{20}$ complexes (Table S1), schematic reaction pathway (Figure S1), and HDR on non-metal-doped C_{20} complex (Table S2) (PDF)

■ AUTHOR INFORMATION

Corresponding Authors

Nadeem S. Sheikh − *Chemical Sciences, Faculty of Science, Universiti Brunei Darussalam, Gadong BE1410, Brunei*

Darussalam; ● orcid.org/0000-0002-0716-7562;
Email: nadeem.sheikh@ubd.edu.bn

Imene Bayach − *Department of Chemistry, College of Science, King Faisal University, Al-Ahsa 31982, Saudi Arabia;*
● orcid.org/0000-0003-1375-0612; Email: ibayach@kfu.edu.sa

Khurshid Ayub − *Department of Chemistry, COMSATS University Islamabad, Abbottabad 22060, Pakistan;*
● orcid.org/0000-0003-0990-1860; Email: khurshid@cuiatd.edu.pk

Authors

Sehrish Sarfaraz − *Department of Chemistry, COMSATS University Islamabad, Abbottabad 22060, Pakistan*

Muhammad Yar − *Department of Chemistry, COMSATS University Islamabad, Abbottabad 22060, Pakistan*

Complete contact information is available at:
https://pubs.acs.org/10.1021/acsomega.3c00721

Notes

The authors declare no competing financial interest.

■ **REFERENCES**

(1) Yang, X.-F.; Wang, A.; Qiao, B.; Li, J.; Liu, J.; Zhang, T. Single-atom catalysts: a new frontier in heterogeneous catalysis. *Acc. Chem. Res.* **2013**, *46*, 1740−1748.

(2) Hagen, J. *Industrial catalysis: a practical approach;* John Wiley & Sons: 2015.

(3) Li, X.; Yang, X.; Huang, Y.; Zhang, T.; Liu, B. Supported Noble-Metal Single Atoms for Heterogeneous Catalysis. *Adv. Mater.* **2019**, *31*, 1902031.

(4) Zhang, S.; Zhang, X.; Rui, Y.; Wang, R.; Li, X. Recent advances in non-precious metal electrocatalysts for pH-universal hydrogen evolution reaction. *Green Energy & Environment* **2021**, *6*, 458−478.

(5) Zhao, W.; Chen, Z.; Yang, X.; Qian, X.; Liu, C.; Zhou, D.; Sun, T.; Zhang, M.; Wei, G.; Dissanayake, P. D.; Ok, Y. S. Recent advances in photocatalytic hydrogen evolution with high-performance catalysts without precious metals. *Renewable Sustainable Energy Rev.* **2020**, *132*, No. 110040.

(6) Bigall, N. C.; Reitzig, M.; Naumann, W.; Simon, P.; van Pée, K. H.; Eychmüller, A. Fungal templates for noble-metal nanoparticles and their application in catalysis. *Am. Ethnol.* **2008**, *120*, 7994−7997.

(7) De Beer, M.; Kunene, A.; Nabaho, D.; Claeys, M.; Van Steen, E. Technical and economic aspects of promotion of cobalt-based Fischer-Tropsch catalysts by noble metals-a review. *J. South. Afr. Inst. Min. Metall.* **2014**, *114*, 157−165.

(8) Shah, A. B.; Sarfaraz, S.; Yar, M.; Sheikh, N. S.; Hammud, H. H.; Ayub, K. Remarkable Single Atom Catalyst of Transition Metal (Fe, Co & Ni) Doped on C2N Surface for Hydrogen Dissociation Reaction. *Nanomaterials* **2023**, *13*, 29.

(9) Liu, D.; Barbar, A.; Najam, T.; Javed, M. S.; Shen, J.; Tsiakaras, P.; Cai, X. Single noble metal atoms doped 2D materials for catalysis applications. *Appl. Catal., B* **2021**, No. 120389.

(10) Liang, S.; Hao, C.; Shi, Y. The power of single-atom catalysis. *ChemCatChem* **2015**, *7*, 2559−2567.

(11) Chen, F.; Jiang, X.; Zhang, L.; Lang, R.; Qiao, B. Single-atom catalysis: Bridging the homo-and heterogeneous catalysis. *Chin. J. Catal.* **2018**, *39*, 893−898.

(12) Cheng, N.; Sun, X. Single atom catalyst by atomic layer deposition technique. *Chin. J. Catal.* **2017**, *38*, 1508−1514.

(13) Chen, Y.; Ji, S.; Chen, C.; Peng, Q.; Wang, D.; Li, Y. Single-atom catalysts: synthetic strategies and electrochemical applications. *Joule* **2018**, *2*, 1242−1264.

(14) Righi, G.; Magri, R.; Selloni, A. H2 Dissociation on Noble Metal Single Atom Catalysts Adsorbed on and Doped into CeO2 (111). *J. Phys. Chem. C* **2019**, *123*, 9875−9883.

(15) Thiel, W. Computational catalysis—past, present, and future. *Angew. Chem., Int. Ed.* **2014**, *53*, 8605−8613.

(16) Rosen, M. A.; Koohi-Fayegh, S. The prospects for hydrogen as an energy carrier: an overview of hydrogen energy and hydrogen energy systems. *Energy Ecol. Environ.* **2016**, *1*, 10−29.

(17) Zhang, F.; Zhao, P.; Niu, M.; Maddy, J. The survey of key technologies in hydrogen energy storage. *Int. J. Hydrogen Energy* **2016**, *41*, 14535−14552.

(18) Zhou, L.; Zhang, C.; McClain, M. J.; Manjavacas, A.; Krauter, C. M.; Tian, S.; Berg, F.; Everitt, H. O.; Carter, E. A.; Nordlander, P.; Halas, N. J. Aluminum nanocrystals as a plasmonic photocatalyst for hydrogen dissociation. *Nano Lett.* **2016**, *16*, 1478−1484.

(19) Fujitani, T.; Nakamura, I.; Akita, T.; Okumura, M.; Haruta, M. Hydrogen dissociation by gold clusters. *Angewandte Chemie International Edition* **2009**, *48*, 9515−9518.

(20) Guo, Y.; Lang, R.; Qiao, B. Highlights of major progress on single-atom catalysis in 2017. *Catalysts* **2019**, *9*, 135.

(21) Qiao, B.; Wang, A.; Yang, X.; Allard, L. F.; Jiang, Z.; Cui, Y.; Liu, J.; Li, J.; Zhang, T. Single-atom catalysis of CO oxidation using Pt 1/FeO x. *Nat. Chem.* **2011**, *3*, 634−641.

(22) Ghosh, T. K.; Nair, N. N. Rh1/γ-Al2O3 Single-Atom Catalysis of O2 Activation and CO Oxidation: Mechanism, Effects of Hydration, Oxidation State, and Cluster Size. *ChemCatChem* **2013**, *5*, 1811−1821.

(23) Parkinson, G. S. Single-atom catalysis: How structure influences catalytic performance. *Catal. Lett.* **2019**, *149*, 1137−1146.

(24) Ling, C.; Niu, X.; Li, Q.; Du, A.; Wang, J. Metal-Free Single Atom Catalyst for N2 Fixation Driven by Visible Light. *J. Am. Chem. Soc.* **2018**, *140*, 14161−14168.

(25) Cheng, N.; Zhang, L.; Doyle-Davis, K.; Sun, X. Single-atom catalysts: from design to application. *Electrochem. Energy Rev.* **2019**, *2*, 539−573.

(26) Liang, J.-X.; Yang, X.-F.; Wang, A.; Zhang, T.; Li, J. Theoretical investigations of non-noble metal single-atom catalysis: Ni 1/FeO x for CO oxidation. *Catal. Sci. Technol.* **2016**, *6*, 6886−6892.

(27) Sun, T.; Xu, L.; Wang, D.; Li, Y. Metal organic frameworks derived single atom catalysts for electrocatalytic energy conversion. *Nano Res.* **2019**, *12*, 2067−2080.

(28) Ma, D.; Li, T.; Wang, Q.; Yang, G.; He, C.; Ma, B.; Lu, Z. Graphyne as a promising substrate for the noble-metal single-atom catalysts. *Carbon* **2015**, *95*, 756−765.

(29) Ren, S.; Yu, Q.; Yu, X.; Rong, P.; Jiang, L.; Jiang, J. Graphene-supported metal single-atom catalysts: a concise review. *Sci. China Mater.* **2020**, *63*, 903−920.

(30) Fu, J.; Wang, S.; Wang, Z.; Liu, K.; Li, H.; Liu, H.; Hu, J.; Xu, X.; Li, H.; Liu, M. Graphitic carbon nitride based single-atom photocatalysts. *Frontiers of Physics* **2020**, *15*, 1−14.

(31) Papa, V.; Cao, Y.; Spannenberg, A.; Junge, K.; Beller, M. Development of a practical non-noble metal catalyst for hydrogenation of N-heteroarenes. *Nat. Catal.* **2020**, *3*, 135−142.

(32) Franco, F.; Rettenmaier, C.; Jeon, H. S.; Cuenya, B. R. Transition metal-based catalysts for the electrochemical CO 2 reduction: from atoms and molecules to nanostructured materials. *Chem. Soc. Rev.* **2020**, *49*, 6884−6946.

(33) Yan, H.; Lv, H.; Yi, H.; Liu, W.; Xia, Y.; Huang, X.; Huang, W.; Wei, S.; Wu, X.; Lu, J. Understanding the underlying mechanism of improved selectivity in pd1 single-atom catalyzed hydrogenation reaction. *J. Catal.* **2018**, *366*, 70−79.

(34) Wang, W.; Tao, Y.; Fan, J.; Yan, Z.; Shang, H.; Phillips, D. L.; Chen, M.; Li, G. Fullerene−Graphene Acceptor Drives Ultrafast

Carrier Dynamics for Sustainable CdS Photocatalytic Hydrogen Evolution. *Adv. Funct. Mater.* **2022**, *32*, 2201357.

(35) He, T.; Gao, G.; Kou, L.; Will, G.; Du, A. Endohedral metallofullerenes (M@ C60) as efficient catalysts for highly active hydrogen evolution reaction. *J. Catal.* **2017**, *354*, 231−235.

(36) Baei, M. T.; Koohi, M.; Shariati, M. Structure, stability, and electronic properties of AlP nanocages evolved from the world's smallest caged fullerene C20: A computational study at DFT. *J. Mol. Struct.* **2018**, *1159*, 118−134.

(37) Tian, X.-G.; Zhang, Y.; Yang, T.-S. First-principles study of H2 dissociative adsorption reactions on WO3 surfaces. *Acta Phys.-Chim. Sin.* **2012**, *28*, 1063−1069.

(38) Latimer, A. A.; Kulkarni, A. R.; Aljama, H.; Montoya, J. H.; Yoo, J. S.; Tsai, C.; Abild-Pedersen, F.; Studt, F.; Nørskov, J. K. Understanding trends in C−H bond activation in heterogeneous catalysis. *Nat. Mater.* **2017**, *16*, 225−229.

(39) Huang, Z.-F.; Song, J.; Du, Y.; Xi, S.; Dou, S.; Nsanzimana, J. M. V.; Wang, C.; Xu, Z. J.; Wang, X. Chemical and structural origin of lattice oxygen oxidation in Co−Zn oxyhydroxide oxygen evolution electrocatalysts. *Nat. Energy* **2019**, *4*, 329−338.

(40) Frisch, M.; Trucks, G.; Schlegel, H.; Scuseria, G.; Robb, M.; Cheeseman, J.; Scalmani, G.; Barone, V.; Mennucci, B.; Petersson, G. 01; Gaussian., Inc: Wallingford, CT 2009.

(41) Tahir, H.; Kosar, N.; Ayub, K.; Mahmood, T. Outstanding NLO response of thermodynamically stable single and multiple alkaline earth metals doped C20 fullerene. *J. Mol. Liq.* **2020**, *305*, No. 112875.

(42) Ahmadi, R.; Pourkarim, S. Investigation of fullerene (C). *Int. J. Bio-Inorg. Hybr. Nanomater* **2015**, *4*, 249−254.

(43) Osuna, S.; Swart, M.; Sola, M. Dispersion corrections essential for the study of chemical reactivity in fullerenes. *J. Phys. Chem. A* **2011**, *115*, 3491−3496.

(44) Baei, M. T.; Peyghan, A. A.; Bagheri, Z.; Tabar, M. B. B-doping makes the carbon nanocones sensitive towards NO molecules. *Phys. Lett. A* **2012**, *377*, 107−111.

(45) Rastegar, S. F.; Peyghan, A. A.; Soleymanabadi, H. Ab initio studies of the interaction of formaldehyde with beryllium oxide nanotube. *Phys. E* **2015**, *68*, 22−27.

(46) Peyghan, A. A.; Soleymanabadi, H.; Moradi, M. Structural and electronic properties of pyrrolidine-functionalized [60] fullerenes. *J. Phys. Chem. Solids* **2013**, *74*, 1594−1598.

(47) Sarfaraz, S.; Yar, M.; Ans, M.; Gilani, M. A.; Ludwig, R.; Hashmi, M. A.; Hussain, M.; Muhammad, S.; Ayub, K. Computational investigation of a covalent triazine framework (CTF-0) as an efficient electrochemical sensor. *RSC Adv.* **2022**, *12*, 3909−3923.

(48) Sarfaraz, S.; Yar, M.; Ayub, K. Covalent triazine framework (CTF-0) surface as a smart sensing material for the detection of CWAs and industrial pollutants. *Mater. Sci. Semicond. Process.* **2022**, *139*, No. 106334.

(49) Sarfaraz, S.; Yar, M.; Khan, A. A.; Ahmad, R.; Ayub, K. DFT investigation of adsorption of nitro-explosives over C2N surface: Highly selective towards trinitro benzene. *J. Mol. Liq.* **2022**, *352*, No. 118652.

(50) Mukhtar, A.; Sarfaraz, S.; Ayub, K. Organic transformations in the confined space of porous organic cage CC2; catalysis or inhibition. *RSC Adv.* **2022**, *12*, 24397−24411.

(51) Wang, J.; Zhao, B.; Liu, S.; Zhu, D.; Huang, F.; Yang, H.; Guan, H.; Song, A.; Xu, D.; Sun, L.; Xie, H.; Wei, W.; Zhang, W.; Helmer Pedersen, T. Catalytic pyrolysis of biomass with Ni/Fe-CaO-based catalysts for hydrogen-rich gas: DFT and experimental study. *Energy Convers. Manage.* **2022**, *254*, No. 115246.

(52) Kosar, N.; Tahir, H.; Ayub, K.; Gilani, M. A.; Imran, M.; Mahmood, T. Remarkable nonlinear optical response of Mn@C20 (M = Na & K and n = 1−6); a DFT outcome. *Mater. Sci. Semicond. Process.* **2022**, *138*, No. 106269.

(53) Zhu, C.; Xia, H. Carbolong chemistry: a story of carbon chain ligands and transition metals. *Acc. Chem. Res.* **2018**, *51*, 1691−1700.

(54) Rivera Rocabado, D. S.; Aizawa, M.; Noguchi, T. G.; Yamauchi, M.; Ishimoto, T. Uncovering the Mechanism of the Hydrogen

Poisoning on Ru Nanoparticles via Density Functional Theory Calculations. *Catalysts* **2022**, *12*, 331.

(55) Lei, Y.; Pakhira, S.; Fujisawa, K.; Wang, X.; Iyiola, O. O.; Perea López, N. s.; Laura Elías, A.; Pulickal Rajukumar, L.; Zhou, C.; Kabius, B.; Alem, N.; Endo, M.; Lv, R.; Mendoza-Cortes, J. L.; Terrones, M. Low-temperature synthesis of heterostructures of transition metal dichalcogenide alloys (W x Mo1−x S2) and graphene with superior catalytic performance for hydrogen evolution. *ACS Nano* **2017**, *11*, 5103−5112.

(56) Soltani, A.; Javan, M. B.; Hoseininezhad-Namin, M. S.; Tajabor, N.; Lemeski, E. T.; Pourarian, F. Interaction of hydrogen with Pd-and co-decorated C24 fullerenes: density functional theory study. *Synth. Met.* **2017**, *234*, 1−8.

(57) Wang, X.; Liew, K. M. Density functional study of interaction of lithium with pristine and Stone-Wales-defective single-walled silicon carbide nanotubes. *J. Phys. Chem. C* **2012**, *116*, 26888−26897.

(58) Javan, M. B.; Shirdel-Havar, A. H.; Soltani, A.; Pourarian, F. Adsorption and dissociation of H2 on Pd doped graphene-like SiC sheet. *Int. J. Hydrogen Energy* **2016**, *41*, 22886−22898.

(59) Wu, H.; Fan, X.; Kuo, J.-L. Metal free hydrogenation reaction on carbon doped boron nitride fullerene: A DFT study on the kinetic issue. *Int. J. Hydrogen Energy* **2012**, *37*, 14336−14342.

(60) Mahamiya, V.; Shukla, A.; Chakraborty, B. Scandium decorated C24 fullerene as high capacity reversible hydrogen storage material: Insights from density functional theory simulations. *Appl. Surf. Sci.* **2022**, *573*, No. 151389.

(61) Zhang, Z.; Zhou, X.; Liu, C.; Guo, J.; Ning, H. Hydrogen adsorption and dissociation on nickel-adsorbed and -substituted Mg17Al12 (100) surface: A density functional theory study. *Int. J. Hydrogen Energy* **2018**, *43*, 793−800.

(62) Sun, K.; Kohyama, M.; Tanaka, S.; Takeda, S. A Study on the Mechanism for H2 Dissociation on Au/TiO2 Catalysts. *J. Phys. Chem. C* **2014**, *118*, 1611−1617.